Springer

Acta Mechanica Sinica

• RESEARCH PAPER •

Acta Mech. Sin., Vol. 39, 323086 (2023)
https://doi.org/10.1007/s10409-023-23086-x

Analytical instability theory of a liquid jet under a thermal field

Ran Qiao, Kai Mu, and Ting Si*

Department of Modern Mechanics, University of Science and Technology of China, Hefei 230026, China

Received April 6, 2023; accepted April 13, 2023; published online June 6, 2023

Linear temporal instability analysis of a liquid jet emerging into a stationary gas environment under a radial thermal field is carried out in this work. The basic temperature profiles are obtained by solving the heat conduction problem between the liquid jet and the surrounding gas. The normal mode method is utilized to solve the temporal evolution of small disturbance, and an analytical dispersion relation on the growth of disturbance is derived. The inviscid asymptotic solution for the liquid jet is further obtained, which shows the explicit form of disturbance growth rate and also decouples the contribution of surface tension and Marangoni stress on the jet instability. The effects of various controlling parameters on the growth of disturbance for an inviscid liquid jet are investigated through a parametric study. Theoretical results show that the jet instability can be suppressed by increasing the temperature ratio between the liquid jet and the surrounding gas, enhancing the Marangoni stress on the surface, weakening the thermal conduction and decreasing the surface tension. The physical mechanisms of Rayleigh-Plateau instability and Marangoni instability which are responsible for the growth of disturbance are distinguished. Through comparing the inviscid asymptotic solution to the disturbance growth of the viscous jet, the applicable situation for the inviscid asymptotic solution is identified, which gives the Reynolds number ranges of $Re \geq O(10^2)$.

Liquid jet, thermal field, Linear instability analysis, Marangoni stress, Surface tension

Citation: R. Qiao, K. Mu, and T. Si, Analytical instability theory of a liquid jet under a thermal field, Acta Mech. Sin. **39**, 323086 (2023), https://doi.org/10.1007/s10409-023-23086-x

1. Introduction

A liquid jet can be formed when one phase of fluid is injected from the capillary nozzle into the surrounding environment. As the jet develops downstream, it collapses into a series of drops intrinsically due to the hydrodynamic instability. In many industrial applications, the thermal field is always employed to modulate the breakup of liquid jet, such as fuel injection [1-3], fiber coating [4] and ink printing [5, 6]. The thermal field is able to affect the value of surface tension directly. Besides, the temperature gradient on the bulk and surface of the liquid jet leads to the Marangoni flow [7,8]. These thermal effects can manipulate the jet instability jointly.

The liquid jet is inherently unstable due to the Rayleigh-Plateau (R-P) instability, which is named after the pioneering works of Plateau [9] and Rayleigh [10]. For an inviscid liquid jet in vacuum, Rayleigh [10] carried out the linear instability analysis in which the dispersion relation for the growth of disturbance was derived. He found that the hydrodynamical instability induced by surface tension is the major factor for the jet breakup. The wavelength of the dominant disturbance which corresponds to the maximum growth rate is 1.437 times the perimeter of the liquid jet. The theoretical results were found to agree well with the experiments [11, 12]. If the viscosity of liquid jet is considered, the dispersion relation should be modified [13-15]. It was found that the viscosity can suppress the jet instability and enlarge the dominant disturbance wavelength, thus leading to larger size of the droplet produced by jet breakup. If the liquid jet flows with a relatively high velocity, other unstable modes caused by the aerodynamic force can be observed, including the first wind-induced, the second wind-induced, and the atomization

*Corresponding author. E-mail address: tsi@ustc.edu.cn (Ting Si)
Executive Editor: Ming Dong

© The Chinese Society of Theoretical and Applied Mechanics and Springer-Verlag GmbH Germany, part of Springer Nature 2023

modes [16]. When a high speed driving stream exists around the liquid jet, the helical mode is easy to appear as the growth of nonaxisymmetric disturbance can be faster than that of the axisymmetric disturbance [17-19]. Apart from the external shearing field, other extra fields are also utilized to manipulate the breakup process of a liquid jet or sheet, including the electric field [20-22], the optical field [23, 24], the acoustic field [25, 26], and the mechanical actuation [27-32].

The instability characteristics of non-isothermal liquid jet are more complex than those of isothermal liquid jet due to the existence of the thermal field. The energy equation should be considered in the linear instability analysis, which makes the dispersion relation much more complex than that in the isothermal case. As the characteristic scale of the jet radius is much smaller than that of the disturbance wavelength, the one-dimensional slender approximation is widely utilized to analyze the jet instability under thermal field. With spatially varying surface tension, the jet breakup time under thermal diffusion was found to be larger than that of the isothermal jet because the Marangoni flow is weakened by the decay of surface tension gradient [33, 34]. Considering the effect of gravity and heat transfer from the jet to the ambient environment, the nonlinear behaviors of non-isothermal molten metal are investigated, indicating that the effect of heat transfer shortens the intact length of jets by increasing the surface tension [35]. Effects of thermal field and thermophysical properties on the disturbance growth rate were investigated for the liquid thread [36]. The thermocapillary and R-P instability regimes were predicted under the slender-jet approximation, and the theoretical results agreed well with experimental observations [24]. Without considering the Marangoni effect, the linear and non-linear instability behaviors of melted silicon in silica medium were studied [37, 38]. Through comparing the theoretical results with experiments, the non-linear model was identified as the better choice to describe the instability behavior of molten substances. Considering the temperature-dependent surface tension coefficient and viscosity, the influence of thermal modulation on the breakup of jet was examined [39]. It is found that the increase in temperature modulation amplitude and frequency can promote the jet instability and lead to more uniform size of droplets. Furthermore, the bifurcation characteristic of a non-isothermal liquid thread was studied by Chen et al. [40]. They found that the fluid motion triggered by the Marangoni stress can make the liquid thread more stable. As the polymeric materials are widely used in applications such as fiber spinning and crystal production, the breakup behavior of non-Newtonian jet was also studied under the modulation of thermal field [41, 42].

To demonstrate more complex flow phenomena, instability analyses of two-dimensional liquid jets were carried out. The breakup behaviors of non-isothermal cylindrical [43] and non-cylindrical liquid bridges [44] with axisymmetric disturbances were studied numerically. The thermocapillary convection with different aspect ratios and Prandtl numbers were represented. The coupling effect of heat and mass transfer on jet instability was also investigated [45, 46]. To study the effect of the thermal field on the jet instability near pinch-off, the non-linear mathematical description for liquid jet with thermocapillary effect was established [47]. The instability characteristics of this non-linear model were summarised with both in-phase and out-phase thermal disturbances, and influences of controlling parameters on the thermocapillary and capillary-induced instabilities were also analyzed in detail. Apart from the axisymmetric disturbances, the unstable spiral waves in non-isothermal liquid jet and bridge were also identified, and influences of thermocapillary and heat transfer on the growth of non-axisymmetric disturbance were illustrated [48-50]. The instability of thermal convection in a high-Prandtl-number liquid bridge was analyzed numerically and experimentally [51, 52]. Furthermore, the instability behaviors of annular liquid thread or coaxial jet were also investigated, showing more abundant thermal-induced effects on the double-layered surfaces [53-56].

Due to the complexity of solving the two-dimensional liquid jet model, an analytical dispersion relation based on the Navier-Stokes and energy equations is still missing. Moreover, the physical mechanisms on the contribution of different hydrodynamical instabilities (e.g., R-P instability and Marangoni instability) for the liquid jet under a thermal field have not been revealed clearly. All these limitations motivate the current study. In this work, we build the two-dimensional liquid jet model and deduce an analytical solution on the linear instability of the jet based on the reasonable basic state of temperature and velocity. The effect of parameters on the jet instability is studied systematically. The structure of this work is represented as follows. Section 2 gives the formulation of the problem, including the physical model dimensionless parameters, the basic flow, the governing equations and boundary conditions. The dispersion relation and asymptotic solutions of the liquid jet under a thermal field are also given. Section 3 studies the effect of controlling parameters on the jet instability and analyzes the corresponding physical mechanisms. Section 4 gives the main conclusions.

2. Formulation of the problem

2.1 Physical model and dimensionless parameters

We consider a liquid jet injecting from a round capillary nozzle to the stationary ambient gas environment in the cylindri-

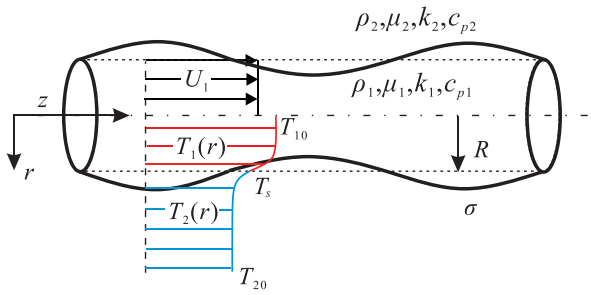

Figure 1 Sketch of a non-isothermal liquid jet emerging into the quiescent surrounding gas environment.

cal coordinate (r, z), as shown in Fig. 1. The liquid jet evolves with radius R and average velocity U_1. The density, dynamical viscosity, thermal conductivity and specific heat capacity of the liquid jet and the surrounding gas are denoted by ρ_i, μ_i, k_i and c_{pi}, where the subscript $i = 1, 2$ stands for the liquid and the gas phase, respectively. The initial temperatures of liquid jet and surrounding gas are defined as T_{10} and T_{20}, respectively. The subscripts 10 and 20 stand for the initial temperature value of the inner liquid and outer surrounding environment. These temperature values are utilized to derive the basic temperature profile in Sect. 2.2. It is notable that the initial temperatures will be used as the initial condition to derive the basic temperature profiles $T_1(r)$ and $T_2(r)$, which will be shown in later section. The surface tension is denoted by σ and varies linearly with the temperature [7,39,44], i.e.,

$$\sigma = \sigma_0 - \gamma(T_s - T_{20}), \tag{1}$$

where $\gamma = -\frac{\mathrm{d}\sigma}{\mathrm{d}T}$ is the rate of the variation of surface tension with temperature, T_s is the temperature on the surface, σ_0 is the surface tension when the temperature of liquid jet equals to that of the surrounding gas. To make the system dimensionless, the characteristic length, velocity, temperature, time, pressure, density, viscosity, thermal conductivity and specific thermal capacity are chosen as $R, U_1, T_{20}, R/U_1, \rho_1 U_1^2, \rho_1, \mu_1, k_1$ and c_{p1}, respectively. The dimensionless parameters involved in the theoretical model include the Reynolds number $Re = \rho_1 R U_1/\mu_1$, the Weber number $We = \rho_1 R U_1^2/\sigma_0$, the Péclet number $Pe = \rho_1 c_{p1} U_1 R/k_1$ and the Marangoni number $Ma = \gamma T_{20}/(\rho_1 R U_1^2)$. The Péclet number is defined by the ratio between the thermal conductive time $\tau_d = R^2\rho_1 c_{p1}/k_1$ and the convective flow time $\tau_c = R/U_1$, which measures the relative importance between the convection effect and the thermal conduction effect. The Marangoni number Ma represents the relative importance of the thermal-induced surface force (i.e., $\gamma T_{20} R$) to the inertia force (i.e., $\rho_1 U_1^2 R^2$). The temperature ratio between the jet and the surrounding gas is denoted by T_r $(= T_{10}/T_{20})$. The physical properties of the gas phase are denoted by the viscosity ratio $\mu_{21} = \mu_2/\mu_1$, the density ratio $\rho_{21} = \rho_2/\rho_1$, the thermal conductivity ratio $k_{21} = k_2/k_1$ and the specific heat capacity ratio $c_{p21} = c_{p2}/c_{p1}$, respectively.

2.2 Basic flow

In linear instability analysis, basic velocity and temperature fields which reflect the real flow characteristics must be given first. For the basic velocity profile, we ignore the velocity boundary layer at the surface and assume a dimensionless uniform velocity $\bar{U}_1 = 1$ inside the jet. Note that the overline in this work stands for the basic state. This stratagem has been utilized for the liquid-gas system as the viscosity of the gas is much smaller than that of the liquids [57, 58]. It has been validated that the theoretical results based on the uniform velocity profile agree well with the experimental measurements [12]. As for the basic temperature profile, we derive an analytical solution by solving a thermal conduction problem. The dimensionless thermal conduction equations for the liquid jet and the surrounding gas are

$$\frac{1}{r}\frac{\partial}{\partial r}\left(r\frac{\partial \bar{T}_1}{\partial r}\right) = Pe_1\frac{\partial \bar{T}_1(r,t)}{\partial t}, 0 < r < 1, \tag{2}$$

$$\frac{1}{r}\frac{\partial}{\partial r}\left(r\frac{\partial \bar{T}_2}{\partial r}\right) = Pe_2\frac{\partial \bar{T}_2(r,t)}{\partial t}, r > 1, \tag{3}$$

where $Pe_1 = Pe, Pe_2 = Pe\rho_{21}C_{p21}/k_{21}$, $\bar{T}_1$ and $\bar{T}_2$ stand for the dimensionless basic temperature profiles for the liquid jet and the surrounding gas, respectively. The corresponding boundary conditions are the consistency condition at the axis, the continuity of temperature and heat flux on the surface, and the far field condition, i.e.,

$$\bar{T}_1 < \infty, r = 0, t > 0, \tag{4}$$

$$\bar{T}_1 = \bar{T}_2, r = 1, t > 0, \tag{5}$$

$$\frac{\mathrm{d}\bar{T}_1}{\mathrm{d}r} = k_{21}\frac{\mathrm{d}\bar{T}_2}{\mathrm{d}r}, r = 1, t > 0, \tag{6}$$

$$\bar{T}_2 = 1, r \gg 1, t > 0. \tag{7}$$

The corresponding initial conditions are given as

$$\bar{T}_1 = T_\mathrm{r}, 0 < r < 1, t = 0, \tag{8}$$

$$\bar{T}_2 = 1, r > 1, t = 0. \tag{9}$$

The Laplace transformation is employed to solve the initial-boundary heat conduction problem. The governing equations after Laplace transformation are

$$\frac{1}{r}\frac{\mathrm{d}}{\mathrm{d}r}\left(r\frac{\mathrm{d}\bar{\bar{T}}_1}{\mathrm{d}r}\right) - Pe_1 s\bar{\bar{T}}_1(r,s) + T = 0, 0 < r < 1, \tag{10}$$

$$\frac{1}{r}\frac{\mathrm{d}}{\mathrm{d}r}\left(r\frac{\mathrm{d}\bar{\bar{T}}_2}{\mathrm{d}r}\right) - Pe_2 s\bar{\bar{T}}_2(r,s) + Pe_2 = 0, r > 1, \tag{11}$$

where s is the Laplace variable and $\bar{\bar{T}}$ represents the temperature after Laplace transformation. The general solutions of Eqs. (10) and (11) are

$$\bar{\bar{T}}_1(r,s) = \frac{T_\mathrm{r}}{s} + A_1 I_0(r\sqrt{Pe_1 s}) + B_1 K_0(r\sqrt{Pe_1 s}), \tag{12}$$

$$\bar{\bar{T}}_2(r,s) = \frac{1}{s} + A_2 I_0(r\sqrt{Pe_2 s}) + B_2 K_0(r\sqrt{Pe_2 s}), \tag{13}$$

where I_0 and K_0 stand for the zeroth first and second kinds of the modified Bessel functions, respectively. The coefficients A_i and B_i (i=1, 2) in Eqs. (12) and (13) are determined by the boundary conditions (i.e., Eqs. (4)-(7)). Previous research has proved that when $x \gg |m^2 - 1/4|$, the modified Bessel functions of order m can be approximate simplified as [59]

$$I_m(x) = \frac{e^x}{\sqrt{2\pi x}}[1 + O(x^{-1})] \sim \frac{e^x}{\sqrt{2\pi x}}, \tag{14}$$

$$K_m(x) = \sqrt{\frac{\pi}{2x}}e^{-x}[1 - O(x^{-1})] \sim \sqrt{\frac{\pi}{2x}}e^{-x}. \tag{15}$$

Therefore, the solutions in spectrum space can be transformed as

$$\bar{\bar{T}}_1(r,s) = \frac{T_\mathrm{r}}{s} + (1 - T_\mathrm{r})\, C_1 \sqrt{\frac{1}{r}}\frac{1}{s}\mathrm{e}^{(r-1)\sqrt{Pe_1 s}}, \tag{16}$$

$$\bar{\bar{T}}_2(r,s) = \frac{1}{s} - (1 - T_\mathrm{r})\, C_2 \sqrt{\frac{1}{r}}\frac{1}{s}\mathrm{e}^{(1-r)\sqrt{Pe_2 s}}, \tag{17}$$

where $C_1 = \frac{\sqrt{k_{21}\rho_{21}c_{p21}}}{1+\sqrt{k_{21}\rho_{21}c_{p21}}}$ and $C_2 = \frac{1}{1+\sqrt{k_{21}\rho_{21}c_{p21}}}$.

The basic temperature profiles of the liquid jet and the surrounding gas can be obtained by the inversion of the transformed function from the Laplace variable s to the actual time t, i.e.,

$$\bar{T}_1 = T_\mathrm{r} + (1 - T_\mathrm{r})\, C_1 \sqrt{\frac{1}{r}}\mathrm{erfc}\left[\sqrt{Pe_1}\left(\frac{1-r}{2\sqrt{t}}\right)\right], \tag{18}$$

$$\bar{T}_2 = 1 - (1 - T_\mathrm{r})\, C_2 \sqrt{\frac{1}{r}}\mathrm{erfc}\left[\sqrt{Pe_2}\left(\frac{r-1}{2\sqrt{t}}\right)\right]. \tag{19}$$

Equations (18) and (19) show that the temperatures of liquid jet and gas surrounding will gradually evolve from the initial discontinuous state (i.e., T_r for the jet and 1 for the gas at $t = 0$) to continuous profiles at $t > 0$, and the Péclet number has a significant influence on the evolution of temperature since it is the direct measurement on the degree of thermal conduction. In the temporal instability analysis, a specific basic temperature profile should be given. In our study, the dimensionless time in the time-dependent equations is chosen as unity (corresponding to the dimensional characteristic convective flow time R/U_1). As a result, the basic temperature profile employed in the instability analysis can be expressed as

$$\bar{T}_1 = T_\mathrm{r} + (1 - T_\mathrm{r})\, C_1 \sqrt{\frac{1}{r}}\mathrm{erfc}\left[\sqrt{Pe_1}\left(\frac{1-r}{2}\right)\right], \tag{20}$$

$$\bar{T}_2 = 1 - (1 - T_\mathrm{r})\, C_2 \sqrt{\frac{1}{r}}\mathrm{erfc}\left[\sqrt{Pe_2}\left(\frac{r-1}{2}\right)\right]. \tag{21}$$

According to Eq. (20), the basic temperature on the surface can be calculated by

$$\bar{T}_s = \bar{T}_1|_{r=1} = T_\mathrm{r} + (1 - T_\mathrm{r})\, C_1. \tag{22}$$

For the convenience of statement, we refer to the jet with the temperature ratio $T_\mathrm{r} > 1$ as the hot jet and that with the temperature ratio $T_\mathrm{r} < 1$ as the cold jet. Figure 2(a) shows the temperature profiles obtained from Eqs. (20) and (21) under different Pe for a hot jet with $T_\mathrm{r} = 1.2$. The thermophysical parameters are certain at $k_{21} = 0.25$, $\rho_{21} = 0.0013$ and $c_{p21} = 0.05$, corresponding to the situation of a water jet surrounded by air environment. In this situation, the ratio between the Péclet numbers $Pe_2/Pe_1 = \rho_{21}c_{p21}/k_{21} \sim 10^{-4}$, which suggests that the efficiency of the thermal conduction at the surrounding gas is much larger than that of the liquid jet. As a result, the temperature profile is almost uniform inside the liquid jet ($r \le 1$) but varies significantly in the gas environment ($r > 1$). Moreover, the increase of Pe leads to a larger temperature gradient across the interface.

2.3 Dimensionless governing equations and boundary conditions

The dimensionless governing equations include the continuities of mass, momentum, and energy, i.e.,

$$\nabla \cdot \boldsymbol{u}_i = 0, \tag{23}$$

$$\frac{\partial \boldsymbol{u}_i}{\partial t} + (\boldsymbol{u}_i \cdot \nabla)\boldsymbol{u}_i = -\left(\frac{1}{\rho_{21}}\right)^{\delta_{2i}} \nabla p_i + \frac{1}{Re_i}\nabla^2 \boldsymbol{u}_i, \tag{24}$$

$$\frac{\partial T_i}{\partial t} + (\boldsymbol{u}_i \cdot \nabla)\, T_i = \frac{1}{Pe_i}\nabla^2 T_i, \tag{25}$$

where δ is the Kronecker function, $Re_1 = Re$, $Re_2 = \rho_{21}Re/\mu_{21}$, $Pe_1 = Pe$, $Pe_2 = Pe\rho_{21}C_{p21}/k_{21}$.

The corresponding boundary conditions include the consistent condition at the symmetric axis, the kinetic and dy-

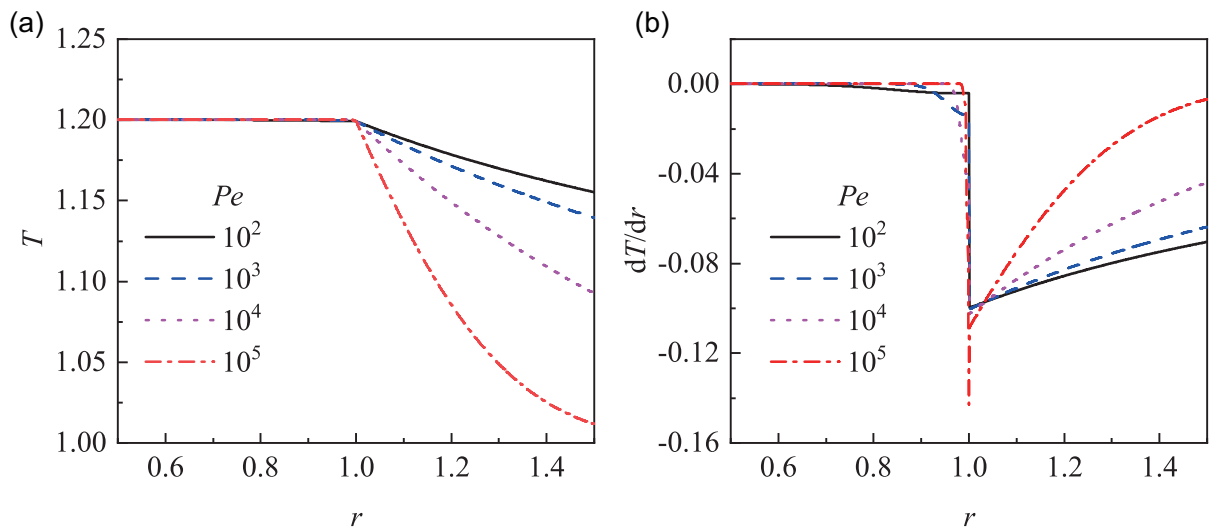

Figure 2 (a) Basic temperature profiles as Péclet number (Pe) varies at a certain temperature ratio $T_{\mathrm{r}} = 1.2$. (b) The rate of change of the temperature $\mathrm{d}T(r)/\mathrm{d}r$ along the radial direction.

namical boundary conditions of the surface, the continuities of temperature and heat flux of the surface, and the far-field conditions, i.e.,

$$\frac{\partial u_1}{\partial r} = \frac{\partial p_1}{\partial r} = \frac{\partial T_1}{\partial r} = v_1 = 0, \text{at } r = 0, \tag{26}$$

$$\frac{\partial S}{\partial t} + \boldsymbol{u}_i \cdot \nabla S = 0, \text{at the surface } S, \tag{27}$$

$$(\boldsymbol{\tau}_2 - \boldsymbol{\tau}_1 \cdot)\, \boldsymbol{n} = \frac{1}{We}(\nabla_s \cdot \boldsymbol{n})\, \boldsymbol{n} + Ma \nabla_s T, \text{at the surface } S, \tag{28}$$

$$\boldsymbol{u}_1 = \boldsymbol{u}_2, T_1 = T_2, \frac{\partial T_1}{\partial r} = k_{21}\frac{\partial T_2}{\partial r}, \text{at the surface } S, \tag{29}$$

$$\boldsymbol{u}_2 = 0,\ p_2 = 0, \text{at } r \to \infty, \tag{30}$$

where $\boldsymbol{\tau}_i = -p_i + \left(\nabla \boldsymbol{u}_i + \nabla^T \boldsymbol{u}_i\right)$, $\nabla_s = (\boldsymbol{I} - \boldsymbol{nn}) \cdot \nabla = \nabla - \boldsymbol{n}\frac{\partial}{\partial n}$ is the tangential gradient operator, and $S = S(r, z, t) = 0$ is a function to describe the position of surface.

In linear stability analysis, the flow variables can be divided into basic quantities and infinitesimal perturbations. Consequently, the velocity components at the axial and radial directions, the pressure and the temperature can be represented as

$$(u_i, v_i, p_i, T_i) = \left(\bar{U}_i, 0, \bar{P}_i, \bar{T}_i\right) + \left(\tilde{u}_i, \tilde{v}_i, \tilde{p}_i, \tilde{T}_i\right), i = 1, 2, \tag{31}$$

where the quantities with bar stand for the basic state and the quantities with tilde are the infinitesimal perturbations. Substituting these flow variables into the dimensionless continuity, momentum and energy equations and keeping the first order of the infinitesimal perturbation, the disturbance equations can be derived as

$$\nabla \cdot \tilde{\boldsymbol{u}}_i = 0, \tag{32}$$

$$\frac{\partial \tilde{\boldsymbol{u}}_i}{\partial t} + (\bar{\boldsymbol{U}}_i \cdot \nabla)\tilde{\boldsymbol{u}}_i + (\tilde{\boldsymbol{u}}_i \cdot \nabla)\bar{\boldsymbol{U}}_i = -\left(\frac{1}{\rho_{21}}\right)^{\delta_{2i}} \nabla \tilde{p}_i + \frac{1}{Re_i}\nabla^2 \tilde{\boldsymbol{u}}_i, \tag{33}$$

$$\frac{\partial \tilde{T}_i}{\partial t} + (\tilde{\boldsymbol{u}}_i \cdot \nabla)\, \bar{T}_i + \left(\bar{\boldsymbol{U}}_i \cdot \nabla\right) \tilde{T}_i = \frac{1}{Pe_i}\nabla^2 \tilde{T}_i. \tag{34}$$

The corresponding boundary conditions are necessary for solving the physical model. At the symmetric axis $r = 0$, the consistency conditions should be satisfied:

$$\frac{\partial \tilde{u}_1}{\partial r} = \frac{\partial \tilde{p}_1}{\partial r} = \frac{\partial \tilde{T}_1}{\partial r} = \tilde{v}_1 = 0. \tag{35}$$

At the disturbed surface $S = r - (1 + \tilde{\eta}) = 0$ (i.e., $r = 1 + \tilde{\eta}$, and $\tilde{\eta}$ is the infinitesimal displacement of the surface), as there is no mass transfer across the surface the kinetic boundary condition should be satisfied:

$$\tilde{v}_1 = \left(\frac{\partial}{\partial t} + \bar{U}_1 \frac{\partial}{\partial z}\right)\tilde{\eta}. \tag{36}$$

The stress balance at the normal and tangential directions on the surface is given as

$$\tilde{p}_2 - \tilde{p}_1 + \frac{2}{Re}\frac{\partial \tilde{v}_1}{\partial r} = \left[\frac{1}{We} - Ma(T_{\mathrm{s}} - 1)\right]\left(1 - k^2\right)\tilde{\eta} + Ma\tilde{T}_1, \tag{37}$$

$$\frac{\partial \tilde{u}_1}{\partial r} + \frac{\partial \tilde{v}_1}{\partial z} = MaRe\frac{\partial \tilde{T}_1}{\partial z}. \tag{38}$$

For the non-isothermal jet, the existence of a thermal field

brings two additional boundary conditions which ensure the continuity of temperature and thermal flux:

$$\tilde{T}_1 + \frac{\partial \bar{T}_1}{\partial r}\tilde{\eta} = \tilde{T}_2 + \frac{\partial \bar{T}_2}{\partial r}\tilde{\eta}, \tag{39}$$

$$\frac{\partial \tilde{T}_1}{\partial r} = k_{21}\frac{\partial \tilde{T}_2}{\partial r}. \tag{40}$$

The far-field conditions at $r \to \infty$ are

$$\tilde{u}_2 = \tilde{v}_2 = \tilde{p}_2 = \tilde{T}_2 = 0. \tag{41}$$

The linear instability analysis is carried out based on the normal mode method. For the liquid jet and the gas surrounding, the perturbation of axial, radial components of velocity $\tilde{u}_i, \tilde{v}_i$, pressure $\tilde{p}_i$, temperature $\tilde{T}_i$ $(i = 1, 2)$, and the displacement of surface $\tilde{\eta}$ can be decomposed into the Fourier form:

$$\left(\tilde{u}_i, \tilde{v}_i, \tilde{p}_i, \tilde{T}_i, \tilde{\eta}\right) = \left(\hat{u}_i, \hat{v}_i, \hat{p}_i, \hat{T}_i, \hat{\eta}\right)\exp\left(\omega t + \mathrm{i}kz\right), \tag{42}$$

where ω stands for the dimensionless complex frequency of the disturbance and k stands for the dimensionless wavenumber. The real and imaginary parts of ω stand for the growth rate and the perturbation frequency of the disturbance, respectively.

For the liquid jet, the velocity vector $\hat{\boldsymbol{u}}_1$ can be decoupled into the inviscid and the viscous parts, i.e., $\hat{\boldsymbol{u}}_1 = \hat{\boldsymbol{u}}_{\mathrm{invis}} + \hat{\boldsymbol{u}}_{\mathrm{vis}}$. Consequently, the governing equations are also decoupled into the inviscid and viscous parts, i.e.,

$$\frac{\partial \hat{\boldsymbol{u}}_{\mathrm{invis}}}{\partial t} + (\bar{\boldsymbol{U}}_1 \cdot \nabla)\hat{\boldsymbol{u}}_{\mathrm{invis}} + (\hat{\boldsymbol{u}}_{\mathrm{invis}} \cdot \nabla)\bar{\boldsymbol{U}}_1 = -\nabla \hat{p}_1, \tag{43}$$

$$\frac{\partial \hat{\boldsymbol{u}}_{\mathrm{vis}}}{\partial t} + (\bar{\boldsymbol{U}}_1 \cdot \nabla)\hat{\boldsymbol{u}}_{\mathrm{vis}} + (\hat{\boldsymbol{u}}_{\mathrm{vis}} \cdot \nabla)\bar{\boldsymbol{U}}_1 = \frac{1}{Re}\nabla^2 \hat{\boldsymbol{u}}_{\mathrm{vis}}. \tag{44}$$

For the inviscid parts, the potential function $\hat{\varphi}_1$ can be introduced, which satisfies $\hat{\boldsymbol{u}}_{\mathrm{invis}} = \nabla\hat{\varphi}_1$. According to Eq. (43), the potential function $\hat{\varphi}$ can be solved as the form:

$$\hat{\varphi}_1 = A_3 I_0(kr) + A_4 K_0(kr). \tag{45}$$

The consistent condition at the axis $r = 0$ gives the coefficient $A_4 = 0$. Therefore, the inviscid parts of perturbation velocity and pressure are

$$\begin{aligned} &\hat{u}_{\mathrm{invis}} = \mathrm{i}kA_3 I_0(kr), \hat{v}_{\mathrm{invis}} = kA_3 I_1(kr), \\ &\hat{p}_1 = (\omega + \mathrm{i}\bar{U}_1 k)A_3 I_0(kr). \end{aligned} \tag{46}$$

As for the disturbance velocity related to the viscosity $\hat{\boldsymbol{u}}_{\mathrm{vis}}$, the governing equation at the radial direction is

$$\frac{\mathrm{d}^2\hat{v}_{\mathrm{vis}}}{\mathrm{d}r^2} + \frac{1}{r}\frac{\mathrm{d}\hat{v}_{\mathrm{vis}}}{\mathrm{d}r} - \left(k^2 + \frac{1}{r^2} + Re\omega + \mathrm{i}Re\bar{U}_1 k\right)\hat{v}_{\mathrm{vis}} = 0. \tag{47}$$

The solution of Eq. (47) is

$$\hat{v}_{\mathrm{vis}} = A_5 I_1(mr) + A_6 K_1(mr), \tag{48}$$

where $m^2 = k^2 + Re(\omega + \mathrm{i}\bar{U}_1 k)$. Similarly, the coefficient $A_6 = 0$ according to the consistent condition at the axis $r = 0$. The axial component can be obtained from the continuity equation, which is

$$\hat{u}_{\mathrm{vis}} = \frac{m}{k}\mathrm{i}A_5 I_0(mr). \tag{49}$$

Adding the solutions of inviscid and viscous parts, the perturbation velocity and pressure for the liquid jet are

$$\begin{aligned} &\hat{u}_1 = \mathrm{i}kA_3 I_0(kr) + \frac{m}{k}\mathrm{i}A_5 I_0(mr), \\ &\hat{v}_1 = kA_3 I_1(kr) + A_5 I_1(mr), \\ &\hat{p}_1 = (\omega + \mathrm{i}\bar{U}_1 k)A_3 I_0(kr). \end{aligned} \tag{50}$$

For the inviscid ambient quiescent gas, the governing equations are

$$\nabla \cdot \hat{\boldsymbol{u}}_2 = 0, \frac{\partial \hat{\boldsymbol{u}}_2}{\partial t} = -\frac{1}{\rho_{21}}\nabla \hat{p}_2. \tag{51}$$

A potential function $\hat{\varphi}_2$ which satisfies $\hat{\boldsymbol{u}}_2 = \nabla\hat{\varphi}_2$ can be introduced as

$$\nabla^2\hat{\varphi}_2 = 0, \hat{p}_2 = -\rho_{21}\frac{\partial \hat{\varphi}_2}{\partial t}. \tag{52}$$

The velocity potential function has a solution as

$$\hat{\varphi}_2 = A_7 I_0(kr) + A_8 K_0(kr). \tag{53}$$

At the jet surface, the kinetic boundary condition should be satisfied:

$$\hat{v}_2 = \omega\hat{\eta}. \tag{54}$$

The far field condition $r \to \infty$ also needs to be satisfied:

$$\hat{v}_2 = 0. \tag{55}$$

Therefore, the coefficients can be determined by Eqs. (54) and (55) as

$$A_7 = 0, A_8 = \frac{\omega}{kK_n'(k)}\hat{\eta}. \tag{56}$$

The perturbation velocity and pressure for the surrounding gas are

$$\hat{u}_2 = \frac{\partial \hat{\varphi}_2}{\partial z} = \mathrm{i}\frac{\omega}{K_1(k)}\hat{\eta}K_0(kr),$$

$$\hat{v}_2 = \frac{\partial \hat{\varphi}_2}{\partial r} = -\frac{\omega}{K_1(k)}\hat{\eta}K_1(kr), \tag{57}$$
$$\hat{p}_2 = -\frac{\rho_{21}\omega^2}{kK_1(k)}K_0(kr)\hat{\eta}.$$

For the disturbed temperature field, the equations of heat transfer are

$$\frac{\mathrm{d}^2\hat{T}_1}{\mathrm{d}r^2} + \frac{1}{r}\frac{\mathrm{d}\hat{T}_1}{\mathrm{d}r} - \left[k^2 + Pe_1\left(\omega + \mathrm{i}\bar{U}_1 k\right)\right]\hat{T}_1 = \frac{\mathrm{d}\bar{T}_1}{\mathrm{d}r}\hat{v}_1,$$
$$\frac{\mathrm{d}^2\hat{T}_2}{\mathrm{d}r^2} + \frac{1}{r}\frac{\mathrm{d}\hat{T}_2}{\mathrm{d}r} - \left(k^2 + Pe_2\omega\right)\hat{T}_2 = \frac{\rho_{21}c_{p21}}{k_{21}}\frac{\mathrm{d}\bar{T}_2}{\mathrm{d}r}\hat{v}_2. \tag{58}$$

The left-hand and right-hand sides of Eq. (58) stand for the effects of thermal conduction and thermal convection, respectively. To obtain the solution of disturbed temperature, we make some simplifications for Eq. (58). As we have obtained the basic temperature profiles $\bar{T}_1$ and $\bar{T}_2$ in Eqs. (20) and (21), their gradient can be further calculated, as shown in Fig. 2(b). It is observed that the values of $\mathrm{d}\bar{T}_1/\mathrm{d}r$ are at the order of $O(10^{-2})$ or less. For the liquid-gas system, the ratios of density ρ_{21}, specific heat capacity c_{p21} and thermal conductivity k_{21} are at the order of $O(10^{-3})$, $O(10^{-2})$ and $O(10^{-1})$, respectively. Therefore, the values of $\left(\rho_{21}c_{p21}/k_{21}\right)\mathrm{d}\bar{T}_2/\mathrm{d}r$ are at the order of $O(10^{-5})$ or less. Consequently, the thermal convection terms on the right-hand side are much smaller than the thermal conduction terms on the left-hand side, which indicates that the right-hand terms of Eq. (58) can be neglected. After neglecting the thermal convection terms, the equations of heat transfer Eq. (58) can be reduced to the equations of thermal conduction as

$$\frac{\mathrm{d}^2\hat{T}_1}{\mathrm{d}r^2} + \frac{1}{r}\frac{\mathrm{d}\hat{T}_1}{\mathrm{d}r} - \left[k^2 + Pe_1\left(\omega + \mathrm{i}\bar{U}_1 k\right)\right]\hat{T}_1 = 0,$$
$$\frac{\mathrm{d}^2\hat{T}_2}{\mathrm{d}r^2} + \frac{1}{r}\frac{\mathrm{d}\hat{T}_2}{\mathrm{d}r} - \left(k^2 + Pe_2\omega\right)\hat{T}_2 = 0. \tag{59}$$

The solutions of Eq. (59) are

$$\hat{T}_1 = A_9 I_0(s_1 r), \hat{T}_2 = A_{10}K_0(s_2 r), \tag{60}$$

where $s_1^2 = k^2 + Pe(\omega + \mathrm{i}\bar{U}_1 k)$, $s_2^2 = k^2 + Pe_2\omega$.

The undetermined coefficients for the perturbation quantities are A_3, A_5, A_9, A_{10} and $\hat{\eta}$. The normal and tangential components of the dynamical boundary conditions, the kinetic boundary condition, and the heat transfer condition at the surface can be employed to obtain the dispersion relation of perturbation growth. Consequently, these boundary conditions can be rewritten as the following form $\boldsymbol{Q}\cdot\boldsymbol{A} = 0$, where $\boldsymbol{A} = [A_3, A_5, A_9, A_{10}, \hat{\eta}]^{\mathrm{T}}$. The dispersion relation can be derived by setting the determinant of $\boldsymbol{Q}$ to zero, i.e., $|\boldsymbol{Q}| = 0$. In this way, we can obtain the dispersion relation:

$$\begin{aligned}
&(\omega + \mathrm{i}k)^2 + \frac{2k^2}{Re}\left[\frac{I_1'(k)}{I_0(k)} + 1\right](\omega + \mathrm{i}k) \\
&+ \frac{4k^3}{Re^2}\left[k\frac{I_1'(k)}{I_0(k)} - m\frac{I_1'(m)}{I_1(m)}\frac{I_1(k)}{I_0(k)}\right] \\
&+ \left[\frac{1}{We} - Ma(T_\mathrm{s} - 1)\right]\frac{I_1(k)}{I_0(k)}k(k^2 - 1) \\
&+ \omega^2\rho_{21}\frac{I_1(k)}{I_0(k)}\frac{K_0(k)}{K_1(k)} + \frac{k_{21}k\varDelta_T Ma I_0(s_1)K_1(s_2)}{I_1(m)I_0(k)} \\
&\cdot\left[I_1(m)\frac{\varDelta_1}{\varDelta_3} + \frac{2}{Re(\omega + \mathrm{i}k)}\frac{\varDelta_2}{\varDelta_3}\right] = 0,
\end{aligned} \tag{61}$$

where

$$\varDelta_1 = kI_0(k) + I_1(k),$$

$$\varDelta_2 = kI_1(m)I_1'(k) - mI_1(k)I_1'(m),$$

$$\varDelta_3 = k_{21}I_0(s_1)K_1(s_1) + \frac{s_1}{s_2}I_1(s_1)K_0(s_1),$$

$$\begin{aligned}
\varDelta_T &= \left[\frac{\mathrm{d}\bar{T}_1}{\mathrm{d}r} - \frac{\mathrm{d}\bar{T}_2}{\mathrm{d}r}\right]_{r=1} \\
&= \frac{(1 - T_\mathrm{r})}{2}\left[C_1\left(2\sqrt{\frac{Pe}{\pi}} - 1\right) - C_2\left(2\sqrt{\frac{Pe}{\pi}\frac{\rho_{21}c_{p21}}{k_{21}}} + 1\right)\right],
\end{aligned}$$

where $C_1 = \frac{\sqrt{k_{21}\rho_{21}c_{p21}}}{1+\sqrt{k_{21}\rho_{21}c_{p21}}}$ and $C_2 = \frac{1}{1+\sqrt{k_{21}\rho_{21}c_{p21}}}$. In order to prove the validity of the dispersion relation Eq. (61), we simplify it to the isothermal case by setting $\varDelta_T = 0, T_\mathrm{s} = 1, \rho_{21} = 0$. Then Eq. (61) can be reduced to

$$\begin{aligned}
&(\omega + \mathrm{i}k)^2 + \frac{2k^2}{Re}\left[\frac{I_1'(k)}{I_0(k)} + 1\right](\omega + \mathrm{i}k) \\
&+ \frac{4k^3}{Re^2}\left[k\frac{I_1'(k)}{I_0(k)} - m\frac{I_1'(m)}{I_1(m)}\frac{I_1(k)}{I_0(k)}\right] \\
&+ \frac{1}{We}\frac{I_1(k)}{I_0(k)}k(k^2 - 1) = 0,
\end{aligned} \tag{62}$$

which is the same as the classical dispersion relation proposed by Lin [60].

We also give some asymptotic solutions of Eq. (61). Considering the approximate expressions of modified Bessel functions given in Eqs. (14) and (15), terms whose independent variables are s_1 or s_2 in Eq. (61) can be simplified once these variables are large numbers compared with 1/4. For the large Péclet number considered in this work ($Pe \geq O(10^2)$), the dispersion relation Eq. (61) can be simplified as

$$\begin{aligned}
&(\omega + \mathrm{i}k)^2 + \frac{2k^2}{Re}\left[\frac{I_1'(k)}{I_0(k)} + 1\right](\omega + \mathrm{i}k) + \frac{4k^3}{Re^2}\left[k\frac{I_1'(k)}{I_0(k)}\right. \\
&\left. - m\frac{I_1'(m)}{I_1(m)}\frac{I_1(k)}{I_0(k)}\right] + \left[\frac{1}{We} - Ma(T_\mathrm{s} - 1)\right]\frac{I_1(k)}{I_0(k)}k(k^2 - 1)
\end{aligned}$$

$$+\omega^2\rho_{21}\frac{I_1(k)}{I_0(k)}\frac{K_0(k)}{K_1(k)}+\frac{k_{21}k\Delta_T Ma}{I_1(m)I_0(k)}\cdot\left[I_1(m)\frac{\Delta_1}{(k_{21}+1)}+\frac{2}{Re(\omega+\mathrm{i}k)}\frac{\Delta_2}{(k_{21}+1)}\right]=0. \tag{63}$$

If we further consider the inviscid limit (i.e., $Re\to\infty$), an asymptotic solution can be obtained, which is

$$(\omega+\mathrm{i}k)^2+\left[\frac{1}{We}-Ma(T_\mathrm{s}-1)\right]\frac{I_1(k)}{I_0(k)}k(k^2-1)+\omega^2\rho_{21}\frac{I_1(k)}{I_0(k)}\frac{K_0(k)}{K_1(k)}+k\Delta_T Ma\left[\frac{k+I_1(k)/I_0(k)}{1+1/k_{21}}\right]=0. \tag{64}$$

Therefore, the perturbation growth rate can be solved in an explicit form:

$$\omega_r=\mathrm{Real}\left\{\frac{\pm\sqrt{-k^2-\xi\left\{-k^2+\left[\frac{1}{We}-Ma(T_\mathrm{s}-1)\right]\frac{I_1(k)}{I_0(k)}k(k^2-1)+k\Delta_T Ma\left[\frac{k+I_1(k)/I_0(k)}{1+1/k_{21}}\right]\right\}}}{\xi}\right\}, \tag{65}$$

where $\xi=\left[1+\rho_{21}\frac{I_1(k)}{I_0(k)}\frac{K_0(k)}{K_1(k)}\right]$. Ignoring the effect of the density of the outer gas in ξ (i.e., $\xi=1$), the growth rate can be finally written as

$$\omega_r=\mathrm{Real}\left\{\pm\sqrt{\left[\frac{1}{We}-Ma(T_\mathrm{s}-1)\right]\frac{I_1(k)}{I_0(k)}k(1-k^2)-k\Delta_T Ma\left[\frac{k+I_1(k)/I_0(k)}{1+1/k_{21}}\right]}\right\}. \tag{66}$$

In the later section, we will mainly study the instability characteristics of an inviscid jet based on the dispersion relation Eq. (66). The effect of viscosity will also be considered by comparing the results between Eqs. (66) and (63). In order to show the physical mechanisms of jet instability, we further rewrite Eq. (66) as the form:

$$\begin{aligned}&\omega_r^2=\mathrm{RHS1}+\mathrm{RHS2},\text{if }\ \mathrm{RHS1}+\mathrm{RHS2}\geq 0,\\&\mathrm{RHS1}=\left[\frac{1}{We}-Ma(T_\mathrm{s}-1)\right]\frac{I_1(k)}{I_0(k)}k(1-k^2),\\&\mathrm{RHS2}=-k\Delta_T Ma\left[\frac{k+I_1(k)/I_0(k)}{1+1/k_{21}}\right],\end{aligned} \tag{67}$$

where RHS1 and RHS2 denote the contribution of the surface tension and the Marangoni stress, respectively. Through comparing the values of RHS1 and RHS2, the relative importance between R-P instability and Marangoni instability can be measured. It is notable that once RHS1 + RHS2 < 0, the square root of RHS1 + RHS2 is an imaginary number. In these cases, the real part of ω equals zero, which means that the liquid jet is neutrally stable.

3. Results and discussions

To understand the effect of various parameters on the instability of an inviscid jet described by the dispersion relation Eq. (66), a reference state must be given first. The reference state should correspond to the real situations in applications, thus ensuring the applicability of the theoretical results. In this work, the diameter of the jet is considered at the scale of order 10^{-4} m and the jet average velocity is approximately 1 m/s. The material of the jet is chosen as the commonly used liquids such as water, silicone oil, ethanol and ethylene glycol. The characteristic density, viscosity, heat specific ratio and thermal conductive coefficient are at the scale of order 10^3 kg/m^3, 10^4 Pa · s, 10^4 J/(kg · K) and 10^{-1} W/(m · K), respectively. The surrounding air is assumed under the room temperature and standard pressure, and the rate of the variation of surface tension with temperature is $\gamma=-\frac{\mathrm{d}\sigma}{\mathrm{d}T}\sim 10^{-2}$ N/(m · K). The ranges of the dimensionless parameters can be estimated based on these assumptions. For convenience, reference values of these dimensionless parameters are chosen as

$$\rho_{21}=0.0013, k_{21}=0.25, C_{p21}=0.05,$$
$$T_\mathrm{r}=1.2, Ma=0.2, Pe=1000, We=5.$$

In the parametric study, we will mainly focus on the variation of T_r, Ma, Pe and We, which are directly related to the temperature field and the flow velocity of the jet. The change of physical parameters (i.e., ρ_{21}, k_{21} and C_{p21}) will not be considered here.

3.1 Effect of temperature ratio on jet instability

The temperature ratio T_r reflects the difference in temperature between the liquid jet and the surrounding gas, which is one of the most prominent parameters for the non-isothermal

liquid jet. Figure 3(a) shows the perturbation growth rate ω_r under different wavenumber k as the temperature ratio gradually changes from 0.6 to 1.4. Note that the results obtained under $T_r = 1$ are the same as the results obtained by the dispersion relation obtained by Rayleigh [10]. Compared with the isothermal case $T_r = 1$, it is represented that the thermal field has an apparent influence on the jet instability. Former studies always consider the spatial distribution of the surface tension to investigate the effect of Marangoni convection on the jet instability [33,34] and the thermal conduction effect is not included in their research. Therefore, the different cases between the hot and cold cases are not included in their study. It can be seen that the growth rate decreases with the increase of temperature ratio in the unstable wavenumber regions where ω_r is larger than zero, suggesting that the increase of temperature ratio will suppress the jet instability. The effect of the temperature ratio on the maximum growth rate ($\omega_{r\text{-max}}$), the most dangerous wavenumber (k_d) which corresponds to the maximum growth rate, and the cut-off wavenumber ($k_{cut\text{-off}}$) are summarized in Fig. 3(b), (c) and (d), respectively. It is notable that $\omega_{r\text{-max}}$, k_d and $k_{cut\text{-off}}$ have been sketched clearly in Fig. 3(a). Figure 3(b) shows that the maximum growth rate decreases with T_r increasing, which means that the instability of the dominant disturbance wave is suppressed with the increase of liquid jet temperature. A smaller $\omega_{r\text{-max}}$ can lead to a longer time of liquid jet breakup and therefore a larger jet breakup length. In Fig. 3(c), it can be observed that the most dangerous wavenumber decreases with the increase of temperature ratio. As the wavenumber is inversely proportional to the perturbation wavelength ($k = 2\pi/\lambda$, where λ is the dimensionless wavelength), a smaller k_d leads to a larger wavelength of interface perturbation on the jet breakup, which results in a larger droplet size as T_r increase. Figure 3(d) shows that the cut-off wavenumber decreases with T_r increasing, which suggests a wider unstable wavenumber region as the temperature of liquid jet decreases. As a consequence, more perturbations with short wavelengths become unstable at a low temperature ratio.

In order to uncover the mechanisms of jet instability, values of RHS1 and RHS2 under different temperature ratios T_r are represented in Fig. 4. As we have stated before, RHS1 and RHS2 represent the contribution of surface tension and Marangoni stress on the perturbation growth rate, respectively. It is observed that the values of RHS1 maintain positive when $k \leq 1$ and become negative as $k > 1$, suggesting that the surface tension can only destabilize the liquid jet whose wavelength is larger than the perimeter of the jet, which is the typical characteristic for the R-P instability. In the unstable wavenumber zone $k \leq 1$, as the temperature ratio

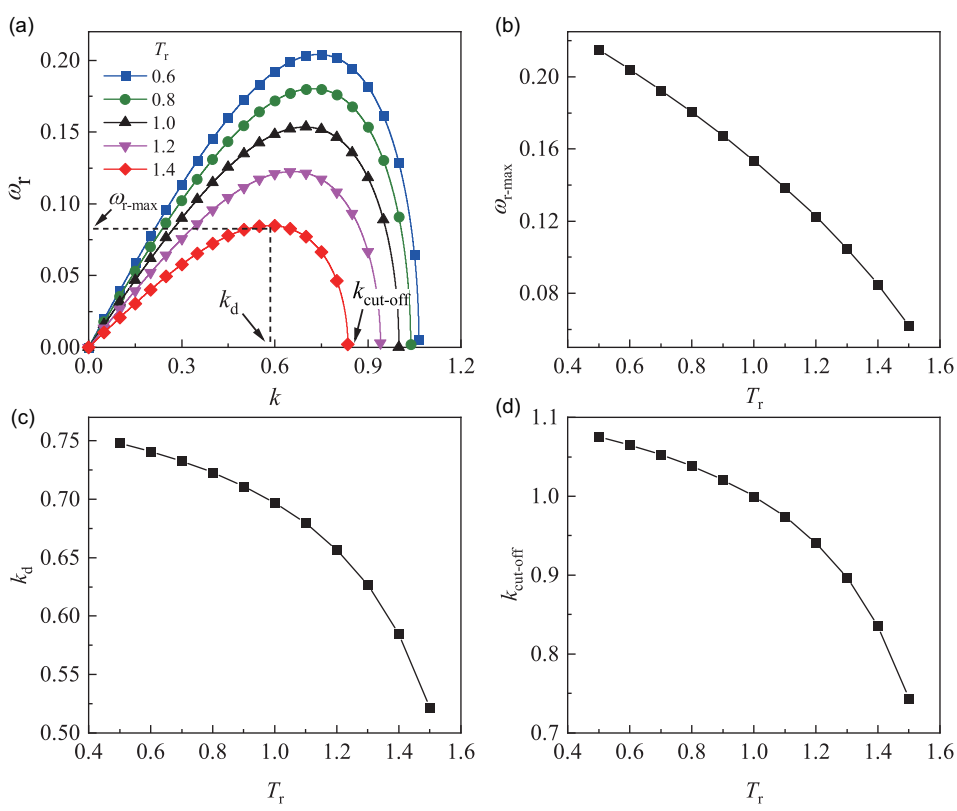

Figure 3 The effects of the temperature ratio T_r on (a) the growth rates ω_r with different wavenumbers k, (b) the maximum growth rate $\omega_{r\text{-max}}$, (c) the most dangerous wavenumber k_d and (d) the cut-off wavenumber $k_{cut\text{-off}}$.

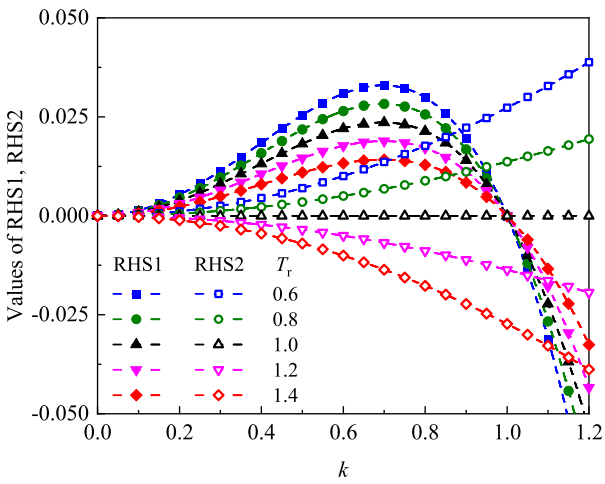

Figure 4 Values of RHS1 and RHS2 under different temperature ratios T_r.

T_r gradually increases, the value of RHS1 decreases significantly. The reason lies in that the interfacial temperature T_s increases with the temperature ratio, causing the decrease of the surface tension at larger T_r. Therefore, the R-P instability is weakened. Once $k > 1$, the values of RHS1 become negative, suggesting a stabilizing role played by surface tension. As for the term RHS2, it is observed that the Marangoni stress does not contribute to the jet instability for the isothermal jet ($T_r = 1$) as RHS2 = 0 invariably. However, the Marangoni stress has opposite influences on jet instability for hot and cold jets due to the contrary signs of RHS2 under these two situations. For the hot jets ($T_r > 1$), the values of RHS2 are negative, which means the Marangoni stress suppresses the breakup of jets. As the absolute value of the RHS2 at $T_r = 1.4$ is always larger than that at $T_r = 1.2$, the stabilizing effect of the Marangoni stress can be enhanced by increasing T_r for hot jets. However, the values of RHS2 are positive for cold jets ($T_r < 1$), which means the Marangoni stress enhances the jet instability. The absolute value of the RHS2 at $T_r = 0.6$ is always larger than that at $T_r = 0.8$, suggesting that the unstabilizing effect of the Marangoni stress can be enhanced by decreasing T_r for cold jets. It is also observed that for a certain T_r, the absolute values of RHS2 become larger as the wavenumber k gradually increases, showing a more significant role played by Marangoni stress in the short wavelength region than that in the long wavelength region. The Marangoni stress is able to manipulate the cut-off wavenumber, resulting in a larger $k_{\text{cut-off}}$ as the temperature ratio T_r decreases.

3.2 Effect of Marangoni number on jet instability

The Marangoni number Ma represents the relative importance between the Marangoni stress on the surface and the inertial stress of the liquid jet. Figure 5(a) represents the pertur-

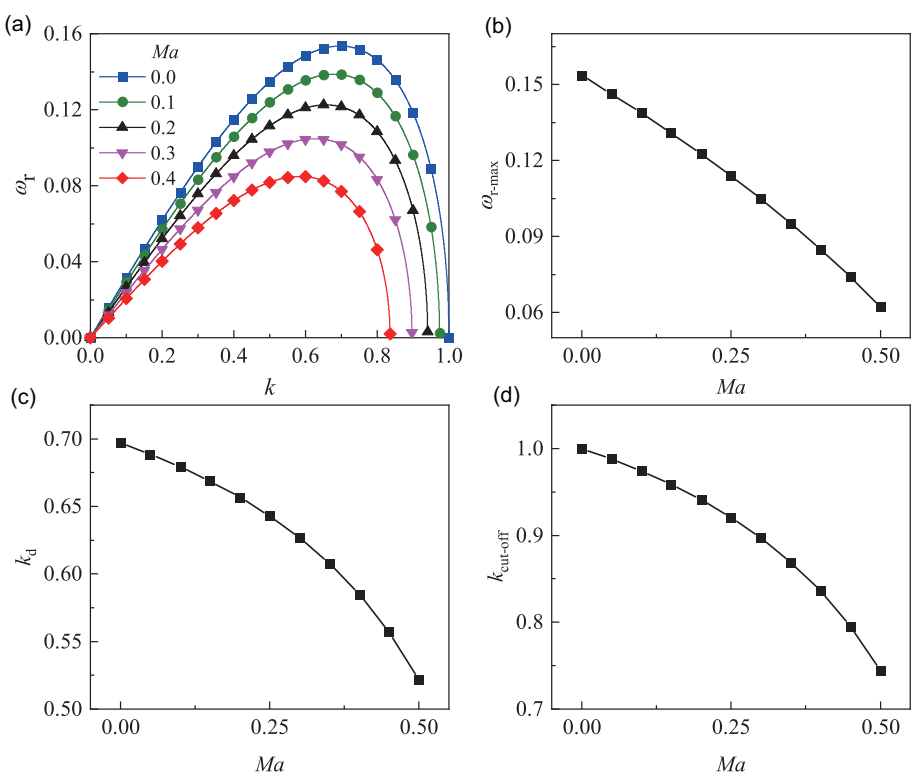

Figure 5 Effects of Marangoni number Ma on (a) the growth rates ω_r with different wavenumbers k, (b) the maximum growth rate $\omega_{r\text{-max}}$, (c) the most dangerous wavenumber k_d, and (d) the cut-off wavenumber $k_{\text{cut-off}}$.

bation growth rates ω_r under different wavenumbers k as the Marangoni number changes from 0 to 0.4 for a hot jet at the certain temperature ratio $T_r = 1.2$. It is shown that the growth rates ω_r decrease with the increase of the Marangoni number in the unstable wavenumber regions, indicating that the increase of Marangoni stress on the surface can suppress the jet instability. The effects of the Marangoni number on the maximum growth rate $\omega_{r\text{-max}}$, the most dangerous wavenumber k_d, and the cut-off wavenumber $k_{\text{cut-off}}$ are displayed in Fig. 5(b), (c), and (d), respectively. As shown in Fig. 5(b), the maximum growth rate decreases with the increase of the Marangoni number, which means that the jet instability is suppressed with the enhancement of the Marangoni stress. Therefore, the breakup time and length of the jet increase obviously as Ma increases. Figure 5(c) represents that the most dangerous wavenumber decreases with Ma increasing, which suggests that the enhancement of the Marangoni stress can result in a larger droplet size. Figure 5(d) shows that the cut-off wavenumber decreases with Ma increasing, which indicates a wider unstable wavenumber region as the Marangoni stress is weakened for a hot jet. As a consequence, more perturbations with short wavelengths become unstable at a low Marangoni number.

To illustrate the physical mechanisms on the effect of Marangoni stress, values of RHS1 and RHS2 under different Marangoni numbers Ma are further given in Fig. 6. Similar to the situations of T_r varying, values of RHS1 are positive when $k \leq 1$ and become negative when $k > 1$, proving that the surface tension can only destabilize the liquid jet as its wavelength is larger than the perimeter of the jet. In the unstable wavenumber region where $k \leq 1$, the value of RHS1 is decreased as the increase of Ma, which is caused by the decrease of the surface tension by the increase of Ma. As a consequence, the R-P instability is weakened. For the term RHS2, it maintains zero when $Ma = 0$ as there is no Marangoni stress on the jet surface. For a nonzero Ma, as the values of RHS2 maintain negative invariably for the hot jet, the Marangoni stress can suppress the breakup of jets. It is found in Fig. 6 that the absolute values of RHS2 increase with the increase of Ma, suggesting that the stabilizing effect of the Marangoni stress can be enhanced. As for a certain Ma, the absolute values of RHS2 become larger as the wavenumber k gradually increases, showing a more significant role played by Marangoni stress in the short wavelength region than that in the long wavelength region. Therefore, the cut-off wavenumber decreases with the increase of Ma, suggesting a narrower instability region of wavelength.

3.3 Effect of thermal conduction on jet instability

The Péclet number Pe is a direct measurement of the relative importance between the thermal convection effect and the thermal conduction effect. The effect of heat conduction on the jet instability was investigated in the previous study under the slender-jet approximation [35], showing that the heat conduction effect will shorten the breakup length of the jet. Based on the full N-S equations and energy equations, the effect of thermal conduction on the jet instability is studied systematically in this section. Figure 7(a) shows the perturbation growth rate ω_r under different wavenumbers k as the Péclet number gradually changes from 10^2 to 10^5. It is observed that the growth rate ω_r will decrease with the increase of the Péclet number in the unstable wavelength region, which indicates that the weakening of the thermal conduction effect will suppress the jet instability. Figure 7(b), (c) and (d) shows the effects of the Péclet number on the maximum growth rate $\omega_{r\text{-max}}$, the most dangerous wavenumber k_d and the cut-off wavenumber $k_{\text{cut-off}}$, respectively. As represented in Fig. 7(b), the maximum growth rate decreases with the increase of the Péclet number, which means that the instability of the dominant disturbance wave is suppressed. Therefore, a longer breakup time and larger length of the liquid jet can be obtained with the increase the of Péclet number. It is observed in Fig. 7(c) that the most dangerous wavenumber decreases with Pe increasing. Therefore, the droplets produced by the breakup of the jet will become larger as the thermal conduction effect is weakened. Figure 7(d) demonstrates that the cut-off wavenumber increases with the decrease of Pe. Consequently, more perturbations with short wavelengths become unstable at a lower Péclet number.

To reveal the physical mechanisms on the effect of thermal conduction and thermal convection on the jet instability, values of RHS1 and RHS2 under different Péclet numbers are shown in Fig. 8. Similarly, values of RHS1 are positive when

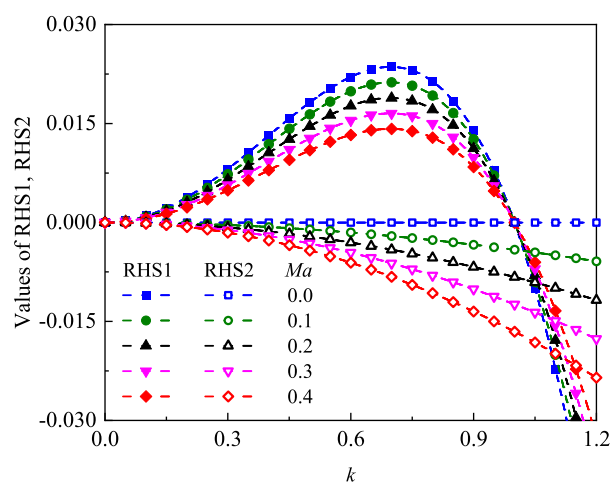

Figure 6 Values of RHS1 and RHS2 under different Marangoni numbers Ma.

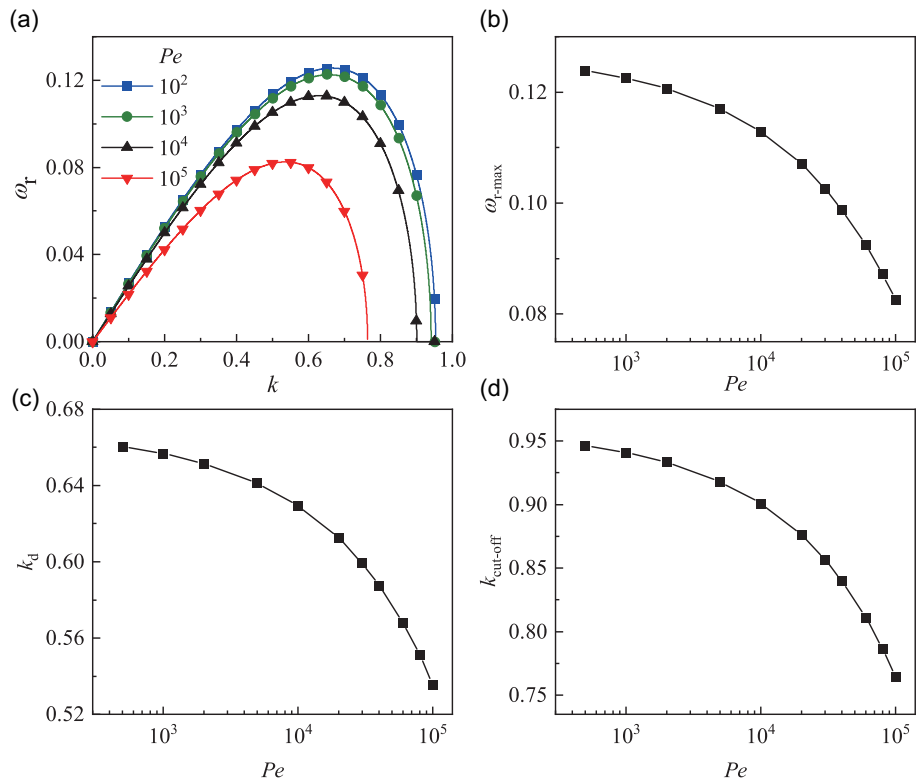

Figure 7 Effects of the Péclet number Pe on (a) the growth rates ω_r with different wavenumbers k, (b) the maximum growth rate $\omega_{r\text{-max}}$, (c) the most dangerous wavenumber k_d, and (d) the cut-off wavenumber $k_{cut\text{-}off}$.

$k \leq 1$ and become negative as $k > 1$. Moreover, the increase of Pe has negligible influence on the value of RHS1 as the temperature T_s on the surface and the surface tension have no relationship with Pe. Therefore, an enhancement of thermal conduction does not affect the R-P instability. The Marangoni stress plays a stabilizing effect on the liquid jet as the values of RHS2 maintain negative invariably. Figure 8 shows that the absolute values of RHS2 get larger with the increase of Pe, indicating that the Marangoni stress plays a more significant role to stabilize the jet under a larger Pe. As for a certain Pe, the absolute values of RHS2 become larger as the wavenumber k gradually increases. Since the jet instability characteristic is determined by the coupling contributions of the surface tension and Marangoni stress, the cut-off wavenumber moves to the long wavenumber region with the increase of Pe.

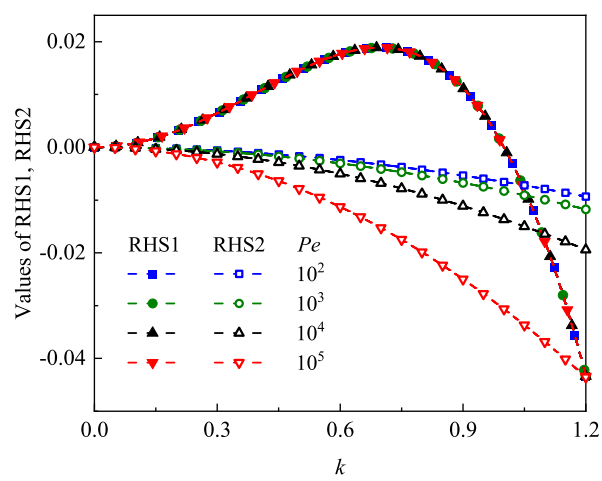

Figure 8 Values of RHS1 and RHS2 under different Péclet numbers Pe. Note that the lines with solid symbols are overlapped.

3.4 Effect of surface tension on jet instability

The Weber number measures the relative importance between the inertial force and the surface tension. Figure 9(a) presents the perturbation growth rate ω_r under different wavenumber k as the Weber number gradually changes from 5 to 15. Without considering the effect of thermal field on the jet instability, the cut-off wavenumber is constant with the variation of the Weber number for the inviscid cases. However, it is shown that the thermal effect makes the unstable wavenumber region change. It is clear that the growth rate decreases with the increase of We in the unstable wavenumber regions, indicating that the decrease of the surface tension can suppress the jet instability. The effects of the Weber number on the maximum growth rate $\omega_{r\text{-max}}$, the most dangerous wavenumber k_d, and the cut-off wavenumber $k_{cut\text{-}off}$ are summarized in Fig. 9(b), (c), and (d), respectively. As repre-

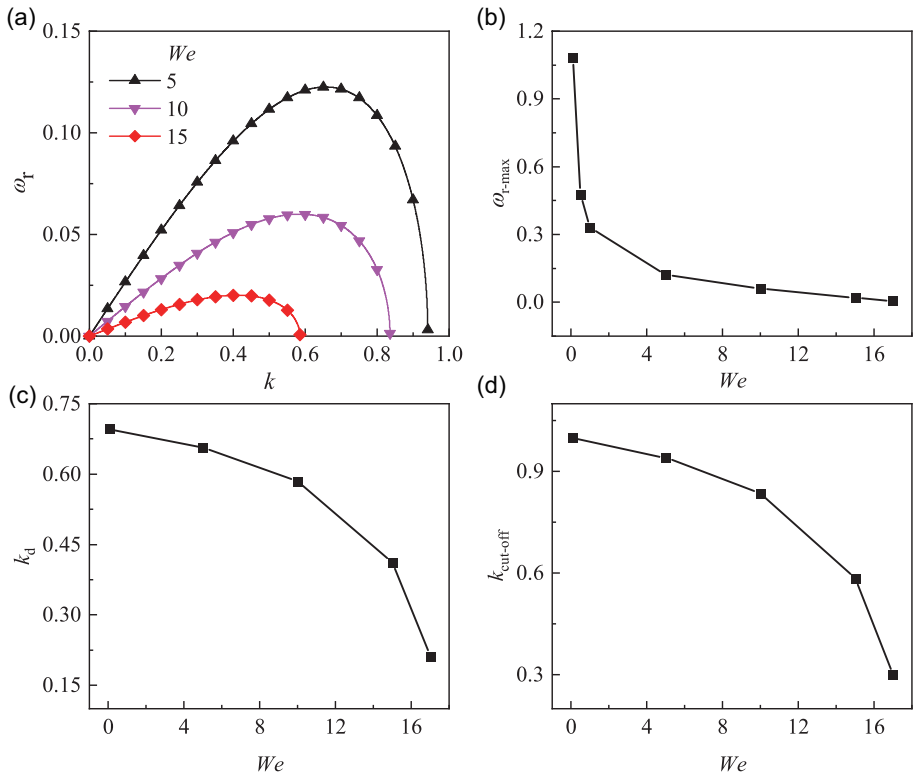

Figure 9 Effects of the Weber number We on (a) the growth rates ω_r with different wavenumbers k, (b) the maximum growth rate $\omega_{r\text{-max}}$, (c) the most dangerous wavenumber k_d, and (d) the cut-off wavenumber $k_{cut\text{-}off}$.

sented in Fig. 9(b), the maximum growth rate decreases with We increasing, which means that with the increase of We. It is shown in Fig. 9(c) that k_d decreases with the increase of the Weber number, which results in a longer perturbation wavelength for jet breakup. Therefore, the droplets produced by the liquid jet will have a larger size as the surface tension is weakened. As for the cut-off wavenumber, Fig. 9(d) shows that $k_{cut\text{-}off}$ decreases with We increasing. Therefore, the unstable wavelength region will be extended to the longer wavelength by decreasing the surface tension.

To reveal the physical mechanisms on the effect of surface tension on jet instability, values of RHS1 and RHS2 under different We are represented in Fig. 10. For the R-P instability represented by RHS1, it is observed that the values of RHS1 are positive when $k \leq 1$ and become negative as $k > 1$. In the unstable region of $k \leq 1$, the value of RHS1 is decreased with the increase of We, suggesting that the decrease of surface tension weakens the R-P instability of the jet. The effect of the Marangoni stress on the jet instability is represented by the value of RHS2. It is clear in Fig. 10 that the change of We only has a negligible influence on the value of RHS2 as the Marangoni stress is invariant to surface tension. Therefore, the coupling contributions of the surface tension and the Marangoni stress shift the cut-off wavenumber to the long wavelength region with the increase of We.

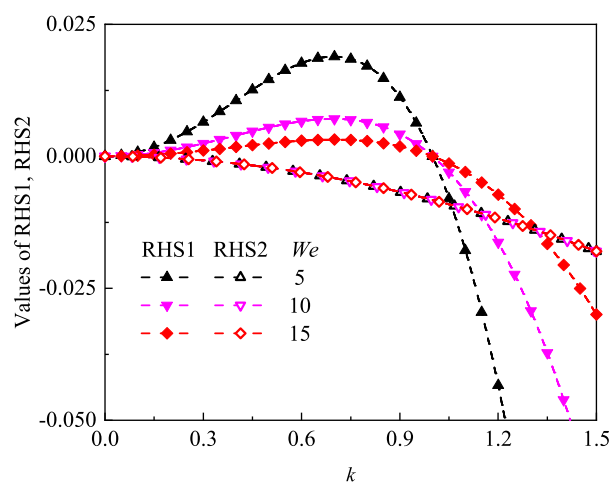

Figure 10 Values of RHS1 and RHS2 under different Weber numbers We. Note that the lines with hollow symbols are overlapped.

3.5 Comparison between inviscid and viscous jets

We also consider the influence of liquid viscosity on the jet instability through comparing the asymptotic inviscid model to the viscous model described by the dispersion relation Eq. (63). Figure 11(a) shows the perturbation growth rate ω_r under different wavenumber k as the Reynolds number Re changes for the viscous model. The growth rate of the

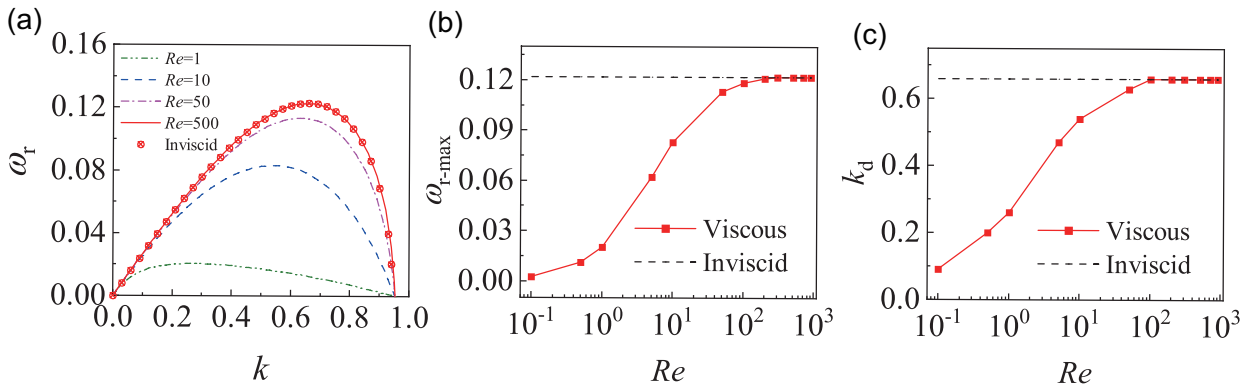

Figure 11 Effects of the Reynolds number *Re* on (a) the growth rate ω_r, (b) the maximum growth rate $\omega_{r\text{-max}}$ and (c) the most dangerous wavenumber k_d. The results obtained from the asymptotic inviscid solution are also given for comparison.

asymptotic inviscid model is also given. The other parameters are certain with the reference state. It is clear that the liquid viscosity does not affect the unstable wavelength region as the cut-off wavenumber of jet instability maintains unchanged at different *Re*. However, the perturbation growth rate decreases significantly with *Re* decreasing, which means that the liquid viscosity can suppress the jet instability. When the Reynolds number is very large (e.g., $Re = 500$), the result calculated from the viscous model almost coincides with that of the inviscid asymptotic solution, suggesting a negligible effect of viscosity. In order to show more details about the effect of Reynolds number, the maximum growth rates $\omega_{r\text{-max}}$ and the corresponding most dangerous wavenumbers k_d at different *Re* are shown in Fig. 11(b) and (c), respectively. When *Re* is larger than a critical value around 200, the values of $\omega_{r\text{-max}}$ and k_d are found to be almost constant and equal to the inviscid asymptotic solution. As *Re* decreases, the results of viscous model gradually diverge from the inviscid model. Specifically, a smaller *Re* leads to smaller values of $\omega_{r\text{-max}}$ and k_d, suggesting that the liquid viscosity can promote the instability of the jet and result in larger droplet size. Based on the results in Fig. 11(b) and (c), we can conclude that the inviscid asymptotic solution is applicable as the Reynolds number is at the order of $Re \geq O(10^2)$.

4. Conclusions

The linear temporal instability analysis of a liquid jet emerging into a stagnant gas under a radial thermal field is carried out in this work. According to the thermal conduction equation and the corresponding initial and boundary conditions, the basic temperature profile is deduced analytically, which shows an almost flattened profile in liquid jet but a significant variation in the gas environment. By dividing the flow variables into basic quantities and small disturbance with the Fourier form, the analytical dispersion relation on the disturbance growth is successfully obtained. The inviscid asymptotic solution of the dispersion relation is further given as the Reynolds number approaches infinity, showing an explicit form of disturbance growth rate. The contribution of R-P instability and Marangoni instability for the inviscid jet is further distinguished by their specific expressions. A parametric study is carried out to investigate the influences of controlling parameters on the jet instability, including the temperature ratio between the liquid jet and the gas environment, the Marangoni number, the Péclet number and the Weber number. The theoretical results show that the jet instability can be suppressed by increasing the temperature ratio between the liquid jet and the surrounding gas, enhancing the Marangoni stress on the surface, weakening the thermal conduction effect and decreasing the surface tension. These parameters are also found to affect the cut-off wavenumber and the dominant wavenumber of jet instability simultaneously. Comparing the disturbance growth of the viscous jet with the inviscid jet, we found that the growth rate obtained by the viscous model gradually converges to the asymptotic solution with the increase of Reynolds number. At the parameter ranges where $Re \geq O(10^2)$, the maximum growth rate and the most dangerous wavenumber obtained by these two models equal each other. This study is expected to provide great insight into the physical mechanism on the instability of a thermal jet in various applications.

Conflict of interest *On behalf of all the authors, the corresponding author states that there is no conflict of interest.*

Author contributions *Ran Qiao carried out the theoretical analysis and wrote the first draft of the manuscript. Kai Mu helped analyze data and organize the manuscript. Ting Si designed the research, reviewed and edited the final version.*

Acknowledgements *This work was supported by the National Natural Science Foundation of China (Grant Nos. 12027801, 11621202, 12272372, and 11902318), and the Youth Innovation Promotion Association of Chinese Academy of Sciences (Grant No. 2018491).*

1 T. C. Lieuwen, Unsteady Combustor Physics (Cambridge University Press, Cambridge, 2012).
2 L. Zhou, Studies on theory and modeling of droplet and spray combustion in China: a review, Acta Mech. Sin. **37**, 1031 (2021).
3 T. Yang, Y. Yin, H. Zhou, and Z. Ren, Review of Lagrangian stochastic models for turbulent combustion, Acta Mech. Sin. **37**, 1467 (2021).
4 J. J. Kaufman, G. Tao, S. Shabahang, E. H. Banaei, D. S. Deng, X. Liang, S. G. Johnson, Y. Fink, and A. F. Abouraddy, Structured spheres generated by an in-fibre fluid instability, Nature **487**, 463 (2012).
5 O. A. Basaran, H. Gao, and P. P. Bhat, Nonstandard inkjets, Annu. Rev. Fluid Mech. **45**, 85 (2013).
6 D. Lohse, Fundamental fluid dynamics challenges in inkjet printing, Annu. Rev. Fluid Mech. **54**, 349 (2022).
7 S. H. Davis, Thermocapillary instabilities, Annu. Rev. Fluid Mech. **19**, 403 (1987).
8 F. Gallaire, and P. T. Brun, Fluid dynamic instabilities: Theory and application to pattern forming in complex media, Phil. Trans. R. Soc. A **375**, 20160155 (2017).
9 J. Plateau, Experimental and Theoretical Statics of Liquids Subject to Molecular Forces Only (Gauthier-Villars, Paris, 1873).
10 L. Rayleigh, On the instability of jets, Proc. Lond. Math. Soc. **1**, 4 (1878).
11 R. J. Donnelly, and W. Glaberson, Experiments on the capillary instability of a liquid jet, Proc. R. Soc. Lond. A **290**, 547 (1966).
12 E. F. Goedde, and M. C. Yuen, Experiments on liquid jet instability, J. Fluid Mech. **40**, 495 (1970).
13 C. Weber, Zum Zerfall eines Flüssigkeitsstrahles, Z. Angew. Math. Mech. **11**, 136 (1931).
14 S. Tomotika, On the instability of a cylindrical thread of a viscous liquid surrounded by another viscous fluid, Proc. R. Soc. Lond. A **150**, 322 (1935).
15 S. Chandrasekhar, Hydrodynamic and Hydromagnetic Stability (Oxford University Press, Oxford, 1961).
16 S. P. Lin, and R. D. Reitz, Drop and spray formation from a liquid jet, Annu. Rev. Fluid Mech. **30**, 85 (1998).
17 J. C. Lasheras, and E. J. Hopfinger, Liquid jet instability and atomization in a coaxial gas stream, Annu. Rev. Fluid Mech. **32**, 275 (2000).
18 J. M. Gordillo, M. Pérez-saborid, and A. M. Gañán-calvo, Linear stability of co-flowing liquid-gas jets, J. Fluid Mech. **448**, 23 (2001).
19 T. Si, F. Li, X. Y. Yin, and X. Z. Yin, Modes in flow focusing and instability of coaxial liquid-gas jets, J. Fluid Mech. **629**, 1 (2009).
20 T. Si, G. B. Li, X. X. Chen, R. J. Tian, and X. Z. Yin, Experimental investigation on flow modes of electrospinning, Acta Mech. Sin. **28**, 644 (2012).
21 G. Li, X. Luo, T. Si, and R. X. Xu, Temporal instability of coflowing liquid-gas jets under an electric field, Phys. Fluids **26**, 054101 (2014).
22 D. Deshawar, and P. Chokshi, Stability analysis of a thinning electrified jet under nonisothermal conditions, Phys. Rev. E **103**, 023107 (2021).
23 H. Liu, Z. Wang, L. Gao, Y. Huang, H. Tang, X. Zhao, and W. Deng, Optofluidic resonance of a transparent liquid jet excited by a continuous wave laser, Phys. Rev. Lett. **127**, 244502 (2021).
24 Y. Zhao, D. Wan, X. Chen, X. Chao, and H. Xu, Uniform breaking of liquid-jets by modulated laser heating, Phys. Fluids **33**, 044115 (2021).
25 B. Jia, T. Wang, Q. Fu, and L. Yang, Experimental study on the stability and breakup of a planar liquid sheet under a standing wave acoustic field, Phys. Rev. Fluids **7**, 124004 (2022).
26 B. Jia, L. Xie, X. Deng, B. He, L. Yang, and Q. Fu, Experimental study on the oscillatory Kelvin-Helmholtz instability of a planar liquid sheet in the presence of axial oscillating gas flow, J. Fluid Mech. **959**, A18 (2023).
27 K. Mu, T. Si, E. Li, R. X. Xu, and H. Ding, Numerical study on droplet generation in axisymmetric flow focusing upon actuation, Phys. Fluids **30**, 012111 (2018).
28 C. Yang, R. Qiao, K. Mu, Z. Zhu, R. X. Xu, and T. Si, Manipulation of jet breakup length and droplet size in axisymmetric flow focusing upon actuation, Phys. Fluids **31**, 091702 (2019).
29 X. Xu, Z. Zhu, K. Mu, F. Huang, and T. Si, Parametric study on breakup of liquid jet in a gas-driven flow focusing process upon external excitation, Phys. Fluids **34**, 042001 (2022).
30 Y. Lu, J. Wang, and J. Wang, Numerical investigation of efficient synthetic jets generated by multiple-frequency actuating signals, Acta Mech. Sin. **38**, 321177 (2022).
31 J. Luo, S. Lyu, L. Qi, and N. Li, Generation of the small tin-droplet streams with a manipulable droplet spacing via the forced velocity perturbation, Phys. Fluids **35**, 013612 (2023).
32 Y. E. Kamis, S. Prakash, W. P. Breugem, and H. B. Eral, Controlling the breakup of spiralling jets: Results from experiments, nonlinear simulations and linear stability analysis, J. Fluid Mech. **956**, A24 (2023).
33 E. P. Furlani, Temporal instability of viscous liquid microjets with spatially varying surface tension, J. Phys. A-Math. Gen. **38**, 263 (2005).
34 E. P. Furlani, and M. S. Hanchak, Nonlinear analysis of the deformation and breakup of viscous microjets using the method of lines, Int. J. Numer. Meth. Fluids **65**, 563 (2011).
35 D. S. Pillai, P. Narayanan, S. Pushpavanam, T. Sundararajan, A. Jasmin Sudha, and P. Chellapandi, A nonlinear analysis of the effect of heat transfer on capillary jet instability, Phys. Fluids **24**, 124106 (2012).
36 D. He, J. J. Wylie, H. Huang, and R. M. Miura, Extension of a viscous thread with temperature-dependent viscosity and surface tension, J. Fluid Mech. **800**, 720 (2016).
37 S. Mowlavi, I. Shukla, P. T. Brun, and F. Gallaire, Particle size selection in capillary instability of locally heated coaxial fiber, Phys. Rev. Fluids **4**, 064003 (2019), arXiv: 1903.00575.
38 I. Shukla, F. Wang, S. Mowlavi, A. Guyomard, X. Liang, S. G. Johnson, and J. C. Nave, Reduced model for capillary breakup with thermal gradients: Predictions and computational validation, Phys. Fluids **33**, 122003 (2021), arXiv: 2104.11671.
39 Y. E. Kamis, H. B. Eral, and W. P. Breugem, Active control of jet breakup and droplet formation using temperature modulation, Phys. Rev. Fluids **6**, 103903 (2021).
40 Y. J. Chen, R. Abbaschian, and P. H. Steen, Thermocapillary suppression of the Plateau-Rayleigh instability: A model for long encapsulated liquid zones, J. Fluid Mech. **485**, 97 (2003).
41 Z. Gao, and K. Ng, Thermal modulation and breakup of liquid jets, Int. J. Numer. Meth. Fluids **70**, 326 (2012).
42 K. Gupta, and P. Chokshi, Stability analysis of non-isothermal fibre spinning of polymeric solutions, J. Fluid Mech. **851**, 573 (2018).
43 A. Rybicki, and J. M. Floryan, Thermocapillary effects in liquid bridges, I. Thermocapillary convection, Phys. Fluids **30**, 1956 (1987).
44 C. Nienhüser, and H. C. Kuhlmann, Stability of thermocapillary flows in non-cylindrical liquid bridges, J. Fluid Mech. **458**, 35 (2002).
45 B. Jia, L. Xie, X. Cui, L. Yang, and Q. Fu, Linear stability of confined coaxial jets in the presence of gas velocity oscillations with heat and mass transfer, Phys. Fluids **31**, 092101 (2019).
46 B. Jia, L. Yang, L. Xie, Q. Fu, and X. Cui, Linear stability of confined

swirling annular liquid layers in the presence of gas velocity oscillations with heat and mass transfer, Int. J. Heat Mass Transfer **138**, 117 (2019).

47 F. Mashayek, and N. Ashgriz, Nonlinear instability of liquid jets with thermocapillarity, J. Fluid Mech. **283**, 97 (1995).

48 J. J. Xu, and S. H. Davis, Instability of capillary jets with thermocapillarity, J. Fluid Mech. **161**, 1 (1985).

49 H. C. Kuhlmann, and H. J. Rath, Hydrodynamic instabilities in cylindrical thermocapillary liquid bridges, J. Fluid Mech. **247**, 247 (1993).

50 M. Wanschura, V. M. Shevtsova, H. C. Kuhlmann, and H. J. Rath, Convective instability mechanisms in thermocapillary liquid bridges, Phys. Fluids **7**, 912 (1995).

51 T. Yano, M. Hirotani, and K. Nishino, Effect of interfacial heat transfer on basic flow and instability in a high-Prandtl-number thermocapillary liquid bridge, Int. J. Heat Mass Transfer **125**, 1121 (2018).

52 L. M. Carrión, M. A. Herrada, and J. M. Montanero, Influence of the dynamical free surface deformation on the stability of thermal convection in high-Prandtl-number liquid bridges, Int. J. Heat Mass Transfer **146**, 118831 (2020).

53 H. A. Dijkstra, The coupling of Marangoni and capillary instabilities in an annular thread of liquid, J. Colloid Interface Sci. **136**, 151 (1990).

54 H. A. Dijkstra, and P. H. Steen, Thermocapillary stabilization of the capillary breakup of an annular film of liquid, J. Fluid Mech. **229**, 205 (1991).

55 S. Li, R. Yang, K. Mu, X. Luo, and T. Si, Thermal effects on the instability of coaxial liquid jets in the core of a gas stream, Phys. Fluids **31**, 032106 (2019).

56 R. Qiao, K. Mu, X. Luo, and T. Si, Instability and energy budget analysis of viscous coaxial jets under a radial thermal field, Phys. Fluids **32**, 122103 (2020).

57 A. M. Sterling, and C. A. Sleicher, The instability of capillary jets, J. Fluid Mech. **68**, 477 (1975).

58 S. P. Lin, and D. J. Kang, Atomization of a liquid jet, Phys. Fluids **30**, 2000 (1987).

59 M. P. Juniper, The effect of confinement on the stability of non-swirling round jet/wake flows, J. Fluid Mech. **605**, 227 (2008).

60 S. P. Lin, Breakup of Liquid Sheets and Jets (Cambridge University Press, Cambridge, 2003).

热场作用下液体射流的解析不稳定性理论

乔然, 穆恺, 司廷

摘要 本文研究了径向热场作用下静止气体环境内液体射流的线性时间不稳定性问题. 通过求解射流与周围气体之间的热传导问题, 得到基本温度分布. 通过正则模方法求解小扰动随时间的演化, 推导得到扰动增长的解析色散关系, 并得到该解析色散关系的无粘渐近解. 该无粘渐近解解耦了表面张力和Marangoni应力对射流失稳的贡献. 通过参数研究, 探究了不同控制参数对无粘液体射流扰动增长率的影响. 结果表明, 提高射流与周围气体的温度比、增强表面的Marangoni应力、减弱热传导效应或降低表面张力均可抑制射流不稳定性. 此外, 本工作对比了Rayleigh-Plateau不稳定性与Marangoni不稳定性对射流失稳过程的贡献. 通过对比粘性射流扰动增长率与其无粘渐近解, 确定了无粘渐近解的适用范围为雷诺数$Re \geq O(10^2)$.